Shape Analysis of the Human Association Pathways

Authors: Fang-Cheng Yeh[1,2,*]

Affiliations:

[1]Department of Neurological Surgery, University of Pittsburgh School of Medicine, Pittsburgh, Pennsylvania, United States

[2]Department of Bioengineering, University of Pittsburgh, Pittsburgh, Pennsylvania, United States

*Correspondence to:

Fang-Cheng Yeh, M.D. Ph.D.

Department of Neurological Surgery,

Department of Bioengineering,

University of Pittsburgh, Pittsburgh, Pennsylvania

Email: frank.yeh@pitt.edu

Abstract

Shape analysis has been widely used in digital image processing and computer vision, but they have not been utilized to compare the structural characteristics of the human association pathways. Here we used shape analysis to derive length, area, volume, and shape metrics from diffusion MRI tractography and utilized them to study the human association pathways. An augmented fiber tracking combined with automatic segmentation was used to improve reproducibility in tractography. The reliability analysis showed that shape descriptors achieved moderate to good test-retest reliability. Further analysis on association pathways showed left dominance in the arcuate fasciculus, cingulum, uncinate fasciculus, frontal aslant tract, and right dominance in the inferior fronto-occipital fasciculus and inferior longitudinal fasciculus. The superior longitudinal fasciculus has a mixed lateralization profile with different metrics showing either left or right dominance. The analysis of between-subject variations shows that the overall layout of the association pathways does not variate a lot across subjects, as shown by low between-subject variation in length, span, diameter, and radius. In contrast, the area of the pathway innervation region has a considerable between-subject variation. A follow-up analysis is warranted to thoroughly investigate the nature of population variations and their structure-function correlation.

Keywords: diffusion MRI, tractography, automatic fiber tracking, shape analysis, shape descriptor.

Introduction

Deciphering the structural layout of the human brain has been a challenging goal to understand how structure defines the brain function (DeFelipe, 2010). The first connectome study identified structural connection using diffusion MRI fiber tracking (Sporns et al., 2005) and formulated brain connections as a graph to reveal the network topology (Bullmore and Sporns, 2009). Further studies have correlated structural connectivity with brain function in the healthy population or disease population (Fornito et al., 2015). The network analysis tackled the structure-function correlation from a panoramic view, but the shape characteristics and topological pattern of the connecting bundles were mostly ignored, particularly the association pathways in the human brain that control most of the cognitive functions. While there are existing shape analysis studies focused on specific applications, (Corouge et al., 2004; Glozman et al., 2018; Kitchell et al., 2018), there is yet a comprehensive study utilizing shape analysis to investigate the structural characeteristics of the human association pathways.

Here we aim to bridge this information gap by applying a comprehensive shape analysis, including length, area, volume, and shape metrics, to investigate the shape characteristics of the human association pathways. Shape analysis has been widely used in computer vision in a variety of applications to achieve imaging understanding of an object (Costa and Cesar Jr, 2000). The analysis provides the “shape descriptor”—a quantitative measurement that describes one part of the shape characteristics as length, area, and volume. Leveraging shape analysis to investigate tractography, however, faces two technical challenges. First, the existing shape analysis is designed for 2D pixel-based or 3D voxel-based images, whereas tractography is a set of coordinate sequences plotting the simulated routes of brain connections. The definition of shape descriptors, such as length, area, and volume metrics, requires a substantial revision to fit into the tractography context. Second, the reproducibility of tractography has long been an

ongoing issue (Rheault et al., 2020). Without a reliable and reproducible tractography input, the result of shape analysis will be meaningless due to “garbage in, garbage out.”

In this study, we first tackled the reproducibility issue using “parameter saturation,” a strategy that saturates parameter space by using millions of parameter combinations instead of a simple parameter setting for the tractography. Then we combined fiber tracking with an automatic segmentation method based on an expert-vetted tractography atlas (Yeh et al., 2018) to isolate target pathways and exclude irrelevant or false connections. After segmentation, we applied an automatic pruning method called topology-informed pruning (Yeh et al., 2019) to eliminate possible false connections. We integrated these three strategies to map 14 association pathways on a test-retest dataset from the human connectome projects (n=44).

Then we introduced the shape descriptors for the tractography. Figure 1 illustrates the calculation using the left arcuate fasciculus as an example. Figure 1a shows the quantification of the length metrics, including length, span, diameters of the bundle, and radius of the innervation regions. Figure 1b shows the area metrics, including the area of the entire track surface and area of the two end surfaces. Figure 1c shows the volume metrics, including total track volume and trunk volume. Based on these metrics, we further derived “shape metrics,” which are unit free indices, including curl, elongation, and irregularity, to describe the shape characteristics of the association pathways. We examined the reliability of these metrics using the intra-class correlations. This reliability results allowed us to ignore findings with poor reproducibility to ensure the robustness of the results. Then we derived the distribution of shape descriptors to reveal their left-right asymmetry and between-subject variations for the association pathways.

Material and Methods

MRI acquisitions

The test-retest diffusion MRI data were acquired by the Human Connectome Project database (WashU consortium)(Glasser et al., 2016). A total of 44 subjects had repeat diffusion MRI scans. 24 of them were female, and 20 of them were male. The age range was 22- to 35-year-old, and the average age was 30.3. Only one subject was left-handed. The data were acquired using a multishell diffusion scheme with three b-values at 1000, 2000, and 3000 s/mm^2. Each shell had 90 sampling directions. The spatial resolution was 1.25 mm isotropic. The acquisition parameters are detailed in the consortium paper (Glasser et al., 2016).

Diffusion MRI Fiber tracking

The diffusion data were first rotated and interpolated to the ICBM2009 T1W space at 1mm. Here the rotation used a rigid-body transformation without a nonlinear deformation so that the shape features were preserved. The b-table was also rotated accordingly. The purpose of this spatial transformation was to facilitate a direct comparison of the tractography between the repeat scans. The rotated data were then reconstructed using generalized q-sampling imaging (Yeh et al., 2010) with a diffusion sampling length ratio of 1.7. The b-table was checked by an automatic quality control routine to ensure its accuracy (Schilling et al., 2019).

We mapped 14 association pathways, including the left and right arcuate fasciculus (AF), cingulum (C). frontal aslant tract (FAT), inferior fronto-occipital fasciculus (IFOF), inferior longitudinal fasciculus (ILF), superior longitudinal fasciculus (SLF), and uncinate fasciculus (UF). The SLF here included “SLF II” and “SLF III,” as they often form a continuous sheet structure together. “SLF I” was not included because it is often separated from the other two SLF bundles and closely sided with cingulum. The starting region of

the fiber tracking (a.k.a. the seeding region) was defined using the corresponding white matter regions in the HCP842 tractography atlas (Yeh et al., 2018) (nonlinearly registered to the subject's native space). To cope with the reproducibility problem in tractography, we saturated the tracking parameters using a random generator to select a combination of fiber tracking parameters within a working range. The tracking parameters included the anisotropy threshold, angular threshold, step size (a.k.a. the propagation distance). The anisotropy threshold was randomly selected between 0.5 and 0.7 of the Otsu's threshold (Otsu, 1979). The angular threshold was randomly selected between 15 to 90 degrees. The step size was randomly selected between 0.5 to 1.5 voxel distance. The random generator was based on a uniform distribution to select a value from the above parameter range. For each of the 14 association pathways, we initiated 5,000,000 tracking iterations, with each iteration having a unique sample of the parameter combination. The fiber tracking was conducted using a deterministic fiber tracking algorithm (Yeh et al., 2013).

Automatic segmentation and pruning

The generated tracks were further filtered by automatic segmentation and pruning. The track segmentation was based on the HCP842 tractography atlas (Yeh et al., 2018). For each trajectory, we calculated its Hausdorff distance with all trajectories in the tractography atlas (nonlinearly wrapped to the subject space). If the shortest distance was found at a trajectory matching our tracking target, and the distance was smaller than 16 mm, then the trajectory was selected. All selected trajectories were then filtered by topology-informed pruning (TIP)(Yeh et al., 2019) with 20 iterations to remove noisy fibers. For each diffusion MRI scan, we successfully obtained all 14 association pathways, except for one subject, the right arcuate fasciculus was too thin, and pruning iteration was reduced to 10, and in two other subjects, no track was selected in automatic segmentation for the right arcuate fasciculus (both test and retest scans). Further investigations into these two subjects found that the initial fiber tracking did

generate numerous pathways from the right arcuate fasciculus area, but subsequent tract segmentation categorized them as right superior longitudinal fasciculus as the trajectories did not reach the right superior temporal lobe. Thus the analysis related to the right arcuate fasciculus excluded these two subjects. For all track bundles, the shape characteristics were quantified using the following shape analysis. The analysis was conducted on the Pittsburgh Supercomputing Center provided through the XSEDE resource (Towns et al., 2014). The source code is available at http://dsi-studio.labsolver.org with documentation to ensure the reproducibility of this study.

Shape analysis

Table 1 lists the shape descriptors and their definition. A fiber bundle is a set of streamline trajectories that can be represented as 3D coordinate sequences: $\{v_i(t) \mid i = 1,2,3, \ldots n\}$. Here n is the total number of tracks, $v_i(t)$ is a sequence of 3D coordinates representing the trajectory of a track. t is a discrete variable from 1 to m_i, where m_i is the number of the coordinates. The length of a fiber bundle is thus defined as follows:

$$length = \frac{1}{n}\sum_{i=1}^{i=n}\sum_{t=1}^{t=m_i-1}\|v_i(t) - v_i(t+1)\|_2 \quad (1)$$

The span is defined as:

$$span = \sum_{i=1}^{i=n}\|v(1) - v(m_i)\|_2 \quad (2)$$

curl is then defined as:

$$curl = \frac{length}{span} \quad (3)$$

Curl has a range of $[1, \infty)$. A track bundle with a big curl value tends to have a curvy shape, whereas a straight line has a curl value of 1.

Then we voxelized tracks to carry out further shape analysis. All trajectories were first resampled so that for any two consecutive coordinates in any track, $\|v_i(t) - v_i(t+1)\|_2$ was smaller than the voxel size. This resampling allowed us to directly "voxelize" tracks by rounding up all coordinates and removing repeat voxels. To minimize discretization error, we multiplied track coordinates by 4 before rounding up, and any further metrics calculation will consider this scaling effect. The voxelized tracks could be represented by a set of unique voxel coordinates denoted as $T = \{V_i \mid i = 1,2,3, \dots N\}$, where *N* is the total number of unique voxel coordinates. The total track volume could be estimated by the following:

$$volume = N \times voxel\ size \quad (4)$$

Note that due to our previous scaling, the voxel size was 4^3 times smaller than the raw DWI voxel size. The bundle diameter was then approximated using a cylinder model:

$$diameter\ (mm) = 2\sqrt{\frac{volume}{\pi \times length}} \quad (5)$$

The diameter can be used to calculate elongation as a shape metric:

$$elongation = \frac{length}{diameter} \quad (6)$$

To calculate track surface area, we converted the track voxel set T to a 3D volume $V(x,y,z)$, whereas $V(x,y,z) = 1$ if $V(x,y,z) \in T$ and 0 otherwise. This 3D volume enabled us to use morphology operation to identify the "surface voxel," defined as a non-zero voxel that connects to at least one zero-valued voxel among its 26 neighboring voxels. The surface area was then estimated as follows:

$$surface\ area = number\ of\ surface\ voxels \times voxel\ spacing^2 \quad (8)$$

Based on a cylinder model, the irregularity of the surface was then defined as

158 $$irregularity = \frac{surface\ area}{\pi \times diameter \times length} \quad (9)$$

159 A surface area much larger than the expected cylinder surface suggests higher shape irregularity.

160 The rest of the shape analysis then utilized the two end surfaces of a track bundle. One obstacle for end
161 surface analysis was that the coordinates of a track could be sequenced in two opposite directions
162 (antegrade or retrograde), and correctly grouping the endpoints into two "end surfaces" required
163 additional clustering steps. To handle it, we used k-means clustering algorithm with *k*=2 and modified it
164 to satisfy the constraint that the endpoints of the same track will always be in the different clusters.
165 Specifically, all $v_i(1)$ was first assigned to cluster 1 and all $v_i(m_i)$ to cluster 2. Then we computed the
166 mean coordinate for each cluster, and for each track, we re-clustered its two endpoints again using their
167 distance to the mean coordinates. All tracks were repeatedly re-clustered until there was no cluster
168 change for all the endpoints. The coordinates of the clustered endpoints were then rounded up to remove
169 repeat voxel coordinates. This generated two unique sets of discrete voxel coordinates: $E_1 = \{V\}$ and
170 E_2, each of them denoting the voxelized end surfaces of the track bundle. We further checked the mean
171 coordinates of E_1 and E_2 and figure out which of the x-, y-, or z-dimension has the largest distance
172 between the mean coordinates. Without loss of generality, we assigned E_2 to be the end surface that
173 had a larger coordinate value in at this dimension (posterior or superior end of a bundle). The area of E_1
174 or E_2 was then calculated as follows:

175 $$area\ of\ an\ end\ surface = (number\ of\ voxels\ in\ the\ surface\ set) \times (voxel\ spacing)^2 \quad (10)$$

176 The area was calculated separately for each of the end surfaces. The radius of an end surface was then
177 calculated by modeling it as a circle, which has a radius equal to 1/5 of the mean distance to the center:

178 $$radius = 1.5 \times (mean\ distance\ of\ voxels\ to\ the\ center) \quad (11)$$

The irregularity was also calculated as follows using a circle model:

$$irregularity\ of\ an\ end\ surface = \frac{\pi \times radius^2}{area\ of\ the\ end\ surface} \quad (12)$$

The irregularity of a circle is 1, whereas any protrusion or intrusion will increase the irregularity. Last, the end surface coordinates will be used to define the "trunk" of a bundle. We first converted E_1 and E_2 into two 3D volumes of 0-1 valued voxels, respectively. The converted volumes were then analyzed by 3D connected component analysis to isolate the largest region of the surface. The two generated regions were then used as two regions of interest to isolate the main trunk of the fiber bundle and calculate its volume.

For each shape descriptor, the test-retest reliability was calculated using one-way random, single measures intraclass correlation (ICC 1-1). The median value of descriptors from 14 bundles was identified as an overall indicator of the performance. The between-subject variations of each descriptor were quantified using the absolute deviation from the median further divided by the median to facilitate comparison.

Results

Augmented fiber tracking and automatic segmentation

Figure 2a shows the tracking result of the first subject, including the arcuate fasciculus (AF), cingulum (C). frontal aslant tract (FAT), inferior fronto-occipital fasciculus (IFOF), inferior longitudinal fasciculus (ILF), superior longitudinal fasciculus (SLF), and uncinate fasciculus (UF) presented in the left, right, anterior, and superior views. Only the association pathways in the left hemisphere are shown here to facilitate comparison. The tractography matches the known anatomical trajectories of the human association pathways, suggesting the feasibility of the automatic segmentation to obtain clean results

without manual intervention. Figure 2b further shows the left arcuate fasciculus of all 44 subjects, including their test-retest results generated from automatic segmentation. The tractography of the repeat scan is placed immediately on the right of the first scan. The tracking results show C-shaped bundles that match the anatomy of the arcuate fasciculus. The tracking did not require manual intervention or placement of regions. This suggests that high-throughput automatic fiber tracking could be realized to provide a decent tractography result.

Test-retest reliability

Figures 3a and 3b further present the test-retest results of the arcuate fasciculus tractography. We selected three best (Fig. 3a) and three worst (Fig. 3b) performers from our subject pool, as quantified by the differences in the volume between the test-retest scans. The tractography in Figure 3a shows high consistency in the fiber trajectories. The topological pattern of the core bundle is almost identical, though minor differences can still be observed at the details. Figure 3b shows tractography from the three worst performers in the test-retest scans. Although at their worst, the overall tractography still also presents decent consistency. Most of the differences are located in the branches, whereas the core trajectories are still highly consistent.

Figure 3c lists the intraclass correlation (ICC) of shape descriptors for each bundle. The shape descriptors can be categorized into length metrics (light gray), area metrics (gray), volume metrics (dark gray), and shape metrics (white). Good reliability (ICC≥0.75) is labeled by a green circle, and moderate reliability (0.75>ICC≥0.5) is labeled by a yellow circle. Poor reliability (ICC<0.5) is marked by red. Out of 210 bundle-descriptor entries, 120 of them (57.1%) have good reliability, 76 of them (36.2%) have moderate reliability, and 14 of them (6.7%) have poor reliability. More than 90% of the scenarios have moderate to good reliability, suggesting overall good reliability of the shape descriptors. All descriptors have a median ICC value greater than 0.5, and the length metrics perform the best, with a median value of ICC around

0.8. The area and volume metrics are the next, showing the median values of ICC around 0.7~0.8. The shape metrics moderate to good reliability, with curl and elongation performing the best, and irregularity the last. There are poor reliability scenarios in radius, trunk volume, and irregularity that requires precautions. These metrics can have outstanding reliability (ICC>0.9) for some bundles and poor reliability (ICC < 0.5) in the others. This indicates that the application of these three shape descriptors still requires additional precautions for the use-case scenarios to avoid poor reliability conditions.

Normative distribution of shape descriptors and their left-right asymmetry

Figure 4a shows representative examples of large and small metrics values using the left arcuate fasciculus selected from the subject pool, whereas the median values of the shape descriptors are listed and color-coded in Fig. 4b. In Figure 4b, the red color represents a relatively higher value compared with other association pathways. For example, the length of the inferior fronto-occipital fasciculus (IFOF) is marked by red, suggesting their longest length among all association pathways. Similarly, the frontal aslant tract (FAT) has the largest diameters, and the left cingulum (C) has the largest surface area. The left superior longitudinal fasciculus (SLF) has the largest topological irregularity. The median value offers an overview of the structural characteristics of the association pathways.

We further plot the distributions of length and area metrics in Fig.5 for each of the association pathways. The two circles on the right upper corner represent the test-retest reliability of the measures, as listed in Fig.3c. Green color indicates good test-retest reliability (ICC≥0.75), yellowish color indicates moderate reliability (0.75>ICC≥0.5), and red color indicates poor reliability (ICC<0.5). The distributions for the left side bundle are colored by blue, whereas the right colored by red. Paired t-tests were used to test the left-right differences. The p-value results are presented with significance marks (*< 0.05, **<0.01, ***< 0.001), and the percentage differences are also calculated by 100%×(*a*-*b*)/*a*, where *a* is the quantity of the dominance side. The largest and most significant left dominance can be found in the arcuate

246 fasciculus (AF) in the span, diameter, and radius of its anterior end surface. On the next, superior
247 longitudinal fasciculus (SLF), cingulum (C), and uncinate fasciculus (UF) show moderately left dominance
248 at 10~20% in diameter and end surfaces (the poor reliability results in SLF and UF labeled by red circles
249 are ignored). The left frontal aslant tract (FAT) shows a slightly larger radius of the innervation region at
250 the superior frontal lobe. In comparison, the inferior fronto-occipital fasciculus (IFOF) and inferior
251 longitudinal fasciculus (ILF) shows right-dominance only in the radius of the end surfaces with no
252 significant difference in the diameter. Figure 6 further shows the distributions of area and volume metrics
253 for the association pathway bundles. The arcuate fasciculus (AF) shows a large left-dominance in area
254 and volume metrics greater than 50%. On the next, cingulum (C), and uncinate fasciculus (UF) show
255 moderately left dominance at ~20% in area and volume. The frontal aslant tract (FAT) shows only a
256 slightly larger volume in the left hemisphere (14.8%). In comparison, inferior longitudinal fasciculus (ILF)
257 shows moderate right-dominance in the area with no significant difference in the volume. The inferior
258 fronto-occipital fasciculus (IFOF) shows right-dominance in the area of the anterior end surface. The
259 superior longitudinal fasciculus (SLF) has a more complicated lateralization profile, with left dominance
260 in tract area and right dominance at the posterior innervation region and trunk volume. Findings from Figs.
261 5 and 6 show an overall trend of left-dominance in the arcuate fasciculus (AF), cingulum (C), frontal aslant
262 tract (FAT), and uncinate fasciculus (UF), and right dominance in the inferior fronto-occipital fasciculus
263 (IFOF) and inferior longitudinal fasciculus (ILF). The superior longitudinal fasciculus (SLF) has mixed
264 lateralization with different metrics showing either left or right dominance.

265 Figure 7 shows the distribution of shape metrics for the association pathways. The differences between
266 left and right distribution are quantified using Cohen's d. While all pathways present significant left-right
267 differences in different shape metrics. The irregularity metric presents the most significant and largest
268 left-right asymmetry. The arcuate fasciculus (AF), cingulum (C), superior longitudinal fasciculus (SLF),

and uncinate fasciculus (UF) shows substantial left dominance in the irregularity (p-value < 0.001, d > 1.5), while inferior longitudinal fasciculus (ILF) shows right dominance (p < 0.001, d=1.73). The lateralization in shape irregularity seems to correlate with the lateralization of the length metrics.

Between-subject variations

Figure 8 shows the between-subject variations using the absolute deviation. The absolute deviation was calculated by the absolute difference from the median to evaluate the dispersion of the shape descriptors between subjects. The deviation was further divided by the median value of the bundle to facilitate comparison. Furthermore, the overall median value of all bundles is plotted by a blue vertical line, whereas the first and third quantiles are plotted by a red line. As shown in Fig. 8, the length, span, and diameters have small between-subject differences, mostly less than 10% deviations. The variations in diameter are larger for the right arcuate fasciculus (AF_R), likely due to its smallest diameter among all association pathways. The radius and surface also have a similar variation level, with the majority of the deviations lower than 20%. A much larger between-subject variation can be observed for the are of the end surfaces, mostly ranged between 10~40% in the absolute deviation. The overall results suggest that the “layout” of the association pathways seems not to vary a lot across subjects, as shown by low between-subject variation in length, span, diameter, and radius. In contrast, the innervation region has a considerable between-subject variation that may account for most of the individual differences in white matter structure.

Discussion

Here we conducted shape analysis on human association pathways and confirmed its reliability in a test-retest dataset. We derived the distribution of shape descriptors to elucidate lateralization and between-subject variations. The results revealed an overall left dominance in arcuate fasciculus, cingulum,

uncinate, and frontal aslant tract, with the largest lateralization found in the arcuate fasciculus. Cingulum and uncinate fasciculus showed moderate lateralization in either diameter, area, or volume, while the frontal aslant tract showed small lateralization. Right dominance was found in inferior fronto-occipital fasciculus and inferior longitudinal fasciculus. Although there was a widespread left-right asymmetry in all association pathways, the detail lateralization profile varied substantially across bundles, and not all bundles share the same lateralization pattern.

The lateralization found in this study is not new to the neuroscience field. For example, studies have shown lateralization in the arcuate fasciculus (Lebel and Beaulieu, 2009; Vernooij et al., 2007) and the inferior longitudinal fasciculus (Panesar et al., 2018), yet our findings revealed a more sophisticated profile in lateralization. A bundle could have left dominance in one metric and right dominance in another, and a comprehensive profile covering all metrics is needed to investigate the asymmetry fully.

In addition to lateralization, the between-subject variation quantified in this study gave us a glimpse into how white matter structures variate across the population. Our analysis showed that the between-subjects variation was small in length metrics such as length, span, diameter, and radius, whereas the area of the end surfaces had a much larger variation. While the length and span did not vary much (< 10% deviation), the area of the innervation region had a median deviation of 24%, implying a considerable variation in how white matter bundle innervates at the cortical surface.

Technical challenges and limitations

There are still limitations in tractography. Good test-retest reliability in shape analysis only implies the robustness of the algorithm. It does not necessarily guarantee that the results are always correct. The fiber tracking algorithm still has the issue of false-positive and false-negative results. For deterministic fiber tracking, false-negative results are more common, as the ability to capture more delicate branches depends on the spatial resolution and the sensitivity of the data acquisition. There are possibilities that a minor branch was left undetected in both test and retest scans due to the limitation of acquisitions. Last, it is noteworthy that we only have 44 subjects included in the analysis. To further investigate between-subject differences, we are planning a future population-based study to include all 1065 HCP subjects and to describe the normative variation of white matter structures. Nonetheless, there are encouraging reproducibility achieved in this study. We showed that a combination of parameter saturation, automatic track segmentation, and topology-inform pruning could provide good reproducibility. The derived metrics further achieved moderate to good test-retest reliability. By integrating with shape analysis, diffusion MRI has a new option for white matter analysis. It can be used in neurological, psychological, and psychiatric studies to investigate the correlation between white matter architecture correlates and abnormal brain functions, with a hope to decipher how structure defines brain functions.

Acknowledgments

The research reported in this publication was partly supported by NIMH of the National Institutes of Health under award number R56MH113634. The content is solely the responsibility of the authors and does not necessarily represent the official views of the National Institutes of Health. This work used the Extreme Science and Engineering Discovery Environment (XSEDE), which is supported by National Science Foundation grant number ACI-1548562. Data were provided by the Human Connectome Project, WU-

Minn Consortium (Principal Investigators: David Van Essen and Kamil Ugurbil; 1U54MH091657) funded by the 16 NIH Institutes and Centers that support the NIH Blueprint for Neuroscience Research; and by the McDonnell Center for Systems Neuroscience at Washington University.

References

Bullmore, E., Sporns, O., 2009. Complex brain networks: graph theoretical analysis of structural and functional systems. Nat Rev Neurosci 10, 186-198.

Corouge, I., Gouttard, S., Gerig, G., 2004. Towards a shape model of white matter fiber bundles using diffusion tensor MRI. 2004 2nd IEEE International Symposium on Biomedical Imaging: Nano to Macro (IEEE Cat No. 04EX821). IEEE, pp. 344-347.

Costa, L.d.F.D., Cesar Jr, R.M., 2000. Shape analysis and classification: theory and practice. CRC Press, Inc.

DeFelipe, J., 2010. From the connectome to the synaptome: an epic love story. Science 330, 1198-1201.

Fornito, A., Zalesky, A., Breakspear, M., 2015. The connectomics of brain disorders. Nat Rev Neurosci 16, 159-172.

Glasser, M.F., Smith, S.M., Marcus, D.S., Andersson, J.L., Auerbach, E.J., Behrens, T.E., Coalson, T.S., Harms, M.P., Jenkinson, M., Moeller, S., Robinson, E.C., Sotiropoulos, S.N., Xu, J., Yacoub, E., Ugurbil, K., Van Essen, D.C., 2016. The Human Connectome Project's neuroimaging approach. Nat Neurosci 19, 1175-1187.

Glozman, T., Bruckert, L., Pestilli, F., Yecies, D.W., Guibas, L.J., Yeom, K.W., 2018. Framework for shape analysis of white matter fiber bundles. Neuroimage 167, 466-477.

Kitchell, L., Bullock, D., Hayashi, S., Pestilli, F., 2018. Shape Analysis of White Matter Tracts via the Laplace-Beltrami Spectrum. International Workshop on Shape in Medical Imaging. Springer, pp. 195-206.

Lebel, C., Beaulieu, C., 2009. Lateralization of the arcuate fasciculus from childhood to adulthood and its relation to cognitive abilities in children. Human Brain Mapping 30, 3563-3573.

Otsu, N., 1979. A threshold selection method from gray-level histograms. IEEE Trans. Sys., Man., Cyber 9, 62-66.

Panesar, S.S., Yeh, F.-C., Jacquesson, T., Hula, W., Fernandez-Miranda, J.C., 2018. A quantitative tractography study into the connectivity, segmentation and laterality of the human inferior longitudinal fasciculus. Frontiers in neuroanatomy 12, 47.

Rheault, F., De Benedictis, A., Daducci, A., Maffei, C., Tax, C.M.W., Romascano, D., Caverzasi, E., Morency, F.C., Corrivetti, F., Pestilli, F., Girard, G., Theaud, G., Zemmoura, I., Hau, J., Glavin, K., Jordan, K.M., Pomiecko, K., Chamberland, M., Barakovic, M., Goyette, N., Poulin, P., Chenot, Q., Panesar, S.S., Sarubbo, S., Petit, L., Descoteaux, M., 2020. Tractostorm: The what, why, and how of tractography dissection reproducibility. Hum Brain Mapp 41, 1859-1874.

Schilling, K.G., Yeh, F.C., Nath, V., Hansen, C., Williams, O., Resnick, S., Anderson, A.W., Landman, B.A., 2019. A fiber coherence index for quality control of B-table orientation in diffusion MRI scans. Magn Reson Imaging 58, 82-89.

Sporns, O., Tononi, G., Kotter, R., 2005. The human connectome: A structural description of the human brain. PLoS Comput Biol 1, e42.

Towns, J., Cockerill, T., Dahan, M., Foster, I., Gaither, K., Grimshaw, A., Hazlewood, V., Lathrop, S., Lifka, D., Peterson, G.D., 2014. XSEDE: accelerating scientific discovery. Computing in science & engineering 16, 62-74.

Vernooij, M.W., Smits, M., Wielopolski, P., Houston, G., Krestin, G.P., van der Lugt, A., 2007. Fiber density asymmetry of the arcuate fasciculus in relation to functional hemispheric language lateralization in both right-and left-handed healthy subjects: a combined fMRI and DTI study. Neuroimage 35, 1064-1076.

Yeh, F.C., Panesar, S., Barrios, J., Fernandes, D., Abhinav, K., Meola, A., Fernandez-Miranda, J.C., 2019. Automatic Removal of False Connections in Diffusion MRI Tractography Using Topology-Informed Pruning (TIP). Neurotherapeutics 16, 52-58.

Yeh, F.C., Panesar, S., Fernandes, D., Meola, A., Yoshino, M., Fernandez-Miranda, J.C., Vettel, J.M., Verstynen, T., 2018. Population-averaged atlas of the macroscale human structural connectome and its network topology. Neuroimage 178, 57-68.

Yeh, F.C., Verstynen, T.D., Wang, Y., Fernandez-Miranda, J.C., Tseng, W.Y., 2013. Deterministic diffusion fiber tracking improved by quantitative anisotropy. PLoS ONE 8, e80713.

Yeh, F.C., Wedeen, V.J., Tseng, W.Y., 2010. Generalized q-sampling imaging. IEEE Trans Med Imaging 29, 1626-1635.

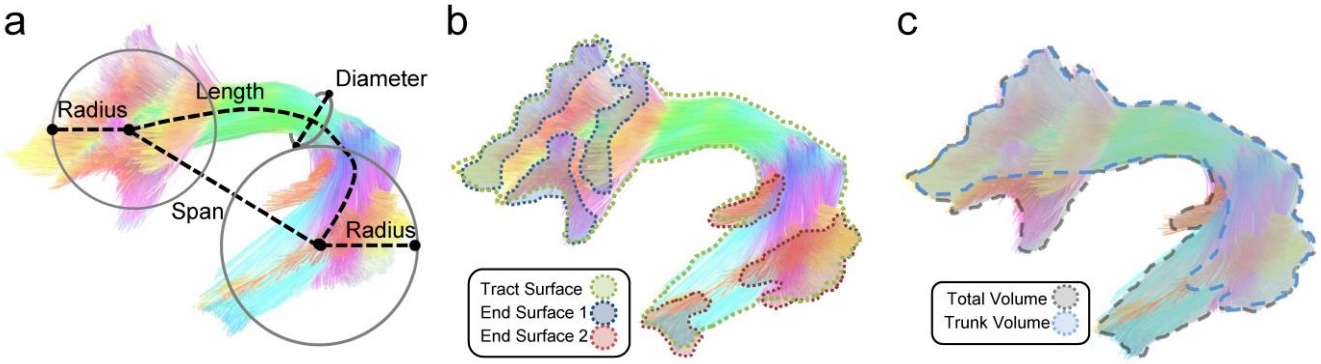

Figure 1. Shape analysis of a bundle and representative examples illustrating high and low values in the shape descriptors. (a) The length metrics include length, span, diameter, and radius of the innervation region. The length measures the length of the bundle trajectory, whereas the span measures the absolute distance between two ends of the bundle. The diameter estimates the average bundle diameter. The radius uses a circular model to estimate the coverage of the innervation regions. (b) The area metrics include total track surface area and area of the two end surfaces. Each fiber bundle has two end surfaces, and their area will be quantified separately. (c) The volume metrics include total volume and trunk volume.

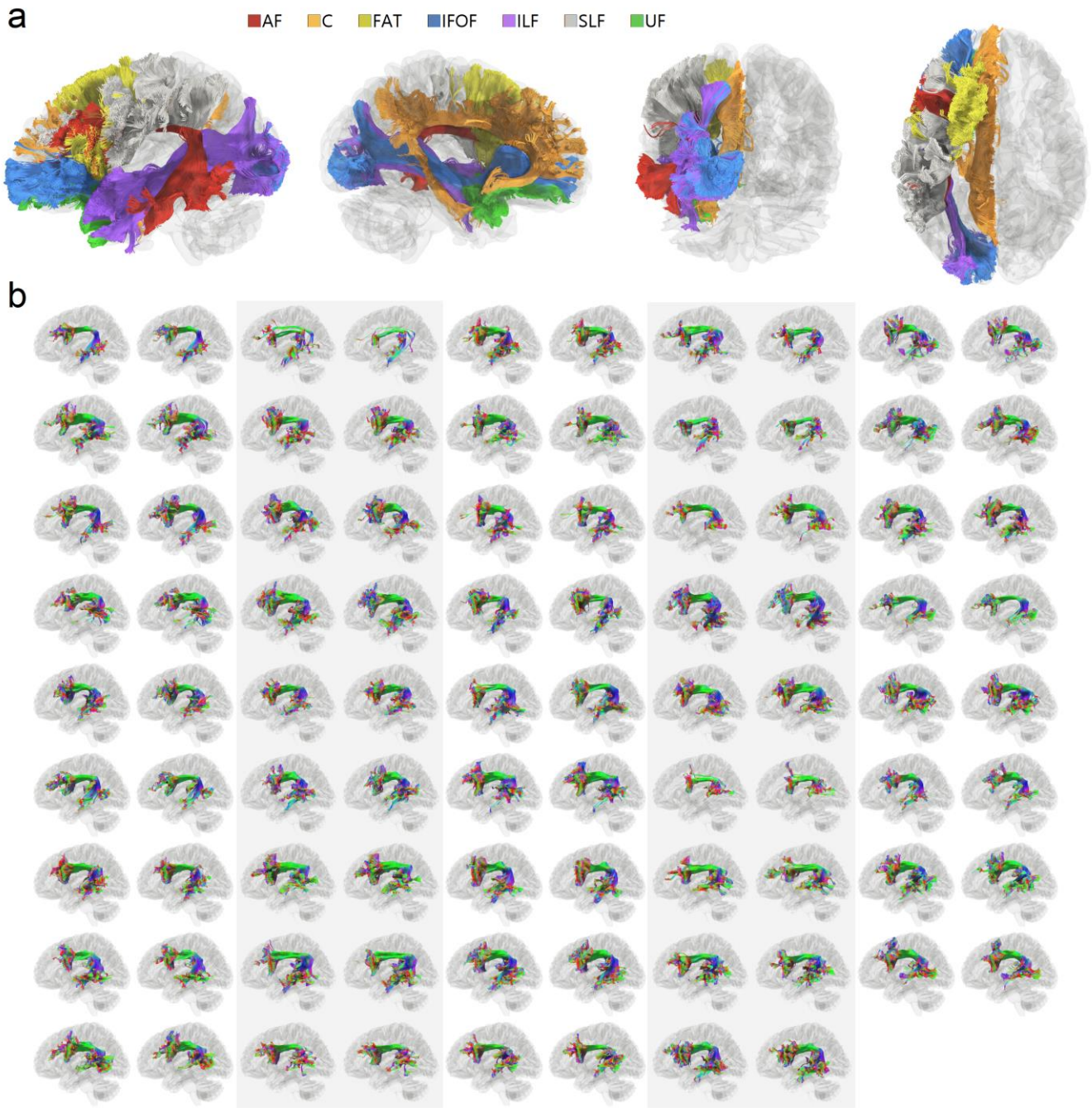

Figure 2. Tractography of human association pathways generated using augmented fiber tracking and automatic segmentation. (a) Seven association pathways in the left hemisphere of a subject are automatically tracked and segmented. The process does not require a manual assignment of regions or editing. The results are consistent with the known neuroanatomical structures. (b) The result of arcuate fasciculus tractography of all test-retest scans (n=44×2) mapped using augmented fiber tracking and

412 automatic segmentation. The retest results are placed on the right of the first scan. All segmentation
413 results show consistent C-shaped bundles. The test-retest results are similar, suggesting the feasibility
414 of the method for high throughput analysis.

415

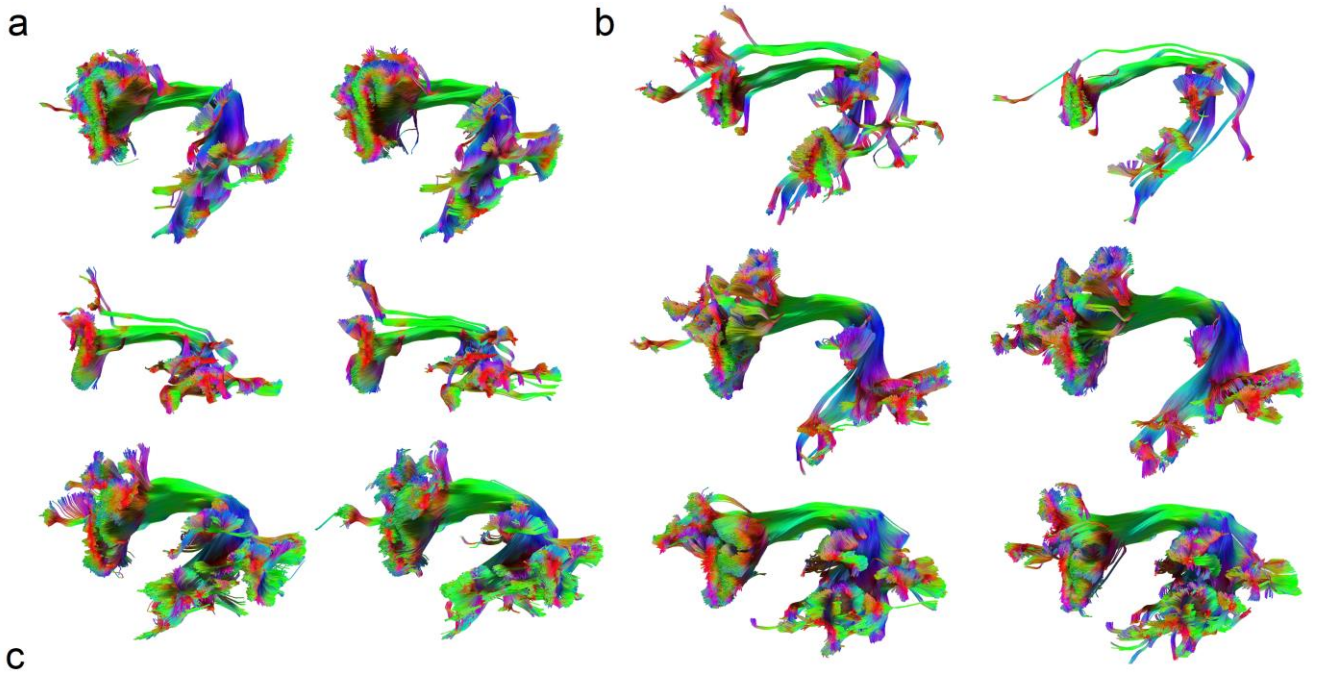

c

	DESCRIPTORS	AF_L	AF_R	C_L	C_R	FAT_L	FAT_R	IFOF_L	IFOF_R	ILF_L	ILF_R	SLF_L	SLF_R	UF_L	UF_R	median
LENGTH	mean length	0.96	0.87	0.85	0.83	0.93	0.97	0.91	0.96	0.69	0.80	0.87	0.87	0.77	0.76	0.87
	span	0.83	0.72	0.88	0.77	0.95	0.96	0.82	0.93	0.66	0.82	0.85	0.92	0.84	0.83	0.83
	diameter	0.88	0.97	0.68	0.65	0.91	0.89	0.71	0.74	0.84	0.81	0.89	0.91	0.70	0.72	0.83
	radius of end1	0.89	0.56	0.76	0.57	0.90	0.80	0.86	0.57	0.66	0.72	0.59	0.91	0.16	0.55	0.69
	radius of end2	0.63	0.80	0.76	0.71	0.92	0.86	0.71	0.81	0.72	0.67	0.38	0.85	0.52	0.41	0.72
AREA	area	0.86	0.95	0.76	0.73	0.88	0.86	0.70	0.76	0.79	0.75	0.88	0.86	0.67	0.71	0.77
	area of end1	0.76	0.95	0.66	0.74	0.90	0.93	0.70	0.79	0.78	0.81	0.92	0.85	0.64	0.56	0.78
	area of end2	0.88	0.93	0.71	0.72	0.92	0.92	0.69	0.67	0.85	0.75	0.91	0.90	0.66	0.69	0.80
VOLUME	volume	0.87	0.96	0.75	0.67	0.90	0.91	0.71	0.79	0.83	0.77	0.90	0.89	0.75	0.74	0.81
	trunk volume	0.75	0.90	0.33	0.67	0.86	0.90	0.70	0.61	0.72	0.36	0.80	0.73	0.72	0.55	0.72
SHAPE	curl	0.83	0.87	0.79	0.54	0.93	0.92	0.73	0.84	0.76	0.70	0.79	0.96	0.89	0.85	0.84
	elongation	0.86	0.91	0.79	0.77	0.90	0.84	0.61	0.65	0.79	0.85	0.86	0.88	0.67	0.75	0.82
	irregularity	0.76	0.91	0.75	0.79	0.76	0.72	0.67	0.64	0.72	0.70	0.70	0.74	0.65	0.52	0.72
	irregularity of end1	0.83	0.03	0.74	0.66	0.95	0.89	0.55	0.30	0.62	0.57	0.48	0.96	0.42	0.50	0.59
	irregularity of end2	0.70	0.61	0.60	0.50	0.89	0.86	0.23	0.30	0.79	0.45	0.48	0.90	0.61	0.37	0.60
	median	0.83	0.90	0.75	0.71	0.90	0.89	0.70	0.74	0.76	0.75	0.85	0.89	0.67	0.69	

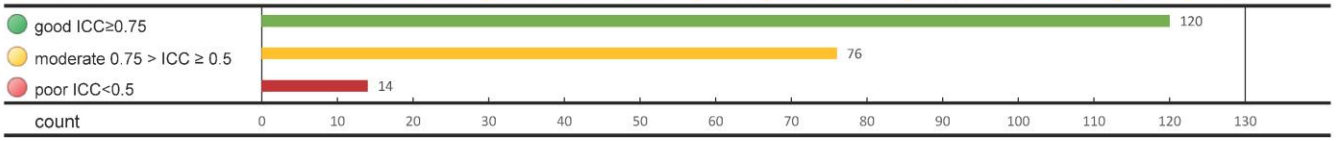

Figure 3. Reproducibility of tractography and reliability of the shape descriptors. (a) Three subjects with the best performing test-retest results are selected for their small differences in volume. The tractography from test and retest scans is of high similarity, while the unique structural characteristics of each subject are preserved. (b) Three subjects with the worst-performing test-retest results are selected as a

421 comparison. Even at its worst, the fiber tracking and segmentation still achieve decent consistency
422 between test-retest scans and preserves the structural characteristics of each subject. (C) The test-retest
423 reliability of the shape descriptors is quantified by intraclass correlation (ICC). The majority of the shape
424 descriptors show moderate (>0.5) to good (>0.75) reliability. The median ICC values for all descriptors
425 are greater than 0.5, while poor reliability (<0.5) still presents in around 6% of the application scenarios.

426

427

a

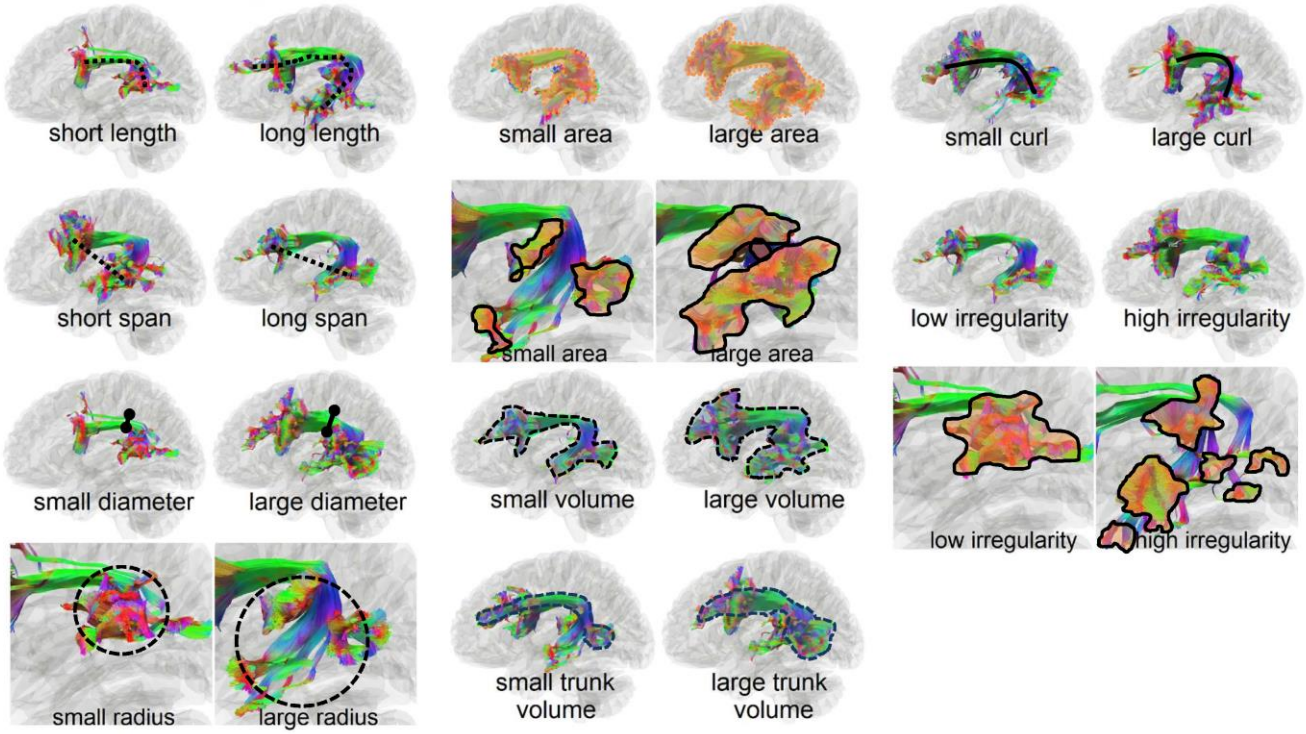

b

	DESCRIPTORS	AF_L	AF_R	C_L	C_R	FAT_L	FAT_R	IFOF_L	IFOF_R	ILF_L	ILF_R	SLF_L	SLF_R	UF_L	UF_R
LENGTH	mean length (mm)	125.6	133.7	111.5	107.8	79.2	76.0	173.2	170.8	122.3	119.3	79.2	97.1	65.0	64.5
	span (mm)	62.3	86.9	77.0	74.3	62.4	58.7	131.1	140.4	102.2	100.9	44.0	60.3	24.4	26.9
	diameter (mm)	14.8	7.8	16.2	14.3	17.8	18.2	12.0	12.0	13.4	13.2	16.6	15.3	15.9	14.2
	radius of end1 (mm)	26.7	13.1	38.6	24.7	21.0	21.2	18.5	23.1	28.6	32.2	26.4	16.3	17.5	22.1
	radius of end2 (mm)	20.3	18.7	39.5	29.4	17.2	15.4	26.3	25.2	19.5	22.6	28.3	24.2	22.2	15.0
AREA	area (10^3 mm^2)	14.4	6.0	15.5	12.9	11.3	10.7	13.5	13.6	12.4	14.1	12.0	11.6	7.8	5.9
	area of end1 (10^3 mm^2)	2.6	0.8	2.7	1.8	2.8	3.1	1.4	1.8	1.9	2.0	1.9	1.9	3.1	2.6
	area of end2 (10^3 mm^2)	2.7	1.0	3.4	2.4	3.0	2.9	2.8	2.7	1.8	1.6	2.7	3.3	3.1	2.7
VOLUME	volume (10^3 mm^3)	21.2	6.4	22.5	18.1	20.1	20.1	20.4	19.2	17.4	16.5	16.8	18.2	13.0	9.9
	trunk volume (10^3 mm^3)	13.9	5.1	7.4	10.2	19.1	17.6	14.2	13.8	8.1	6.8	8.9	13.4	10.7	8.0
SHAPE	curl	2.0	1.6	1.4	1.4	1.3	1.3	1.3	1.2	1.2	1.2	1.8	1.6	2.6	2.4
	elongation	8.3	16.7	6.7	7.4	4.4	4.3	14.4	14.8	9.2	9.1	4.7	6.4	4.0	4.4
	irregularity	5.0	3.6	5.7	5.2	4.9	5.0	4.1	4.1	4.9	5.5	6.1	5.0	4.7	4.1
	irregularity of end1	0.9	0.6	1.8	1.0	0.5	0.4	0.9	0.9	1.3	1.7	1.0	0.5	0.4	0.6
	irregularity of end2	0.5	1.1	1.4	1.1	0.3	0.3	0.7	0.7	0.7	0.9	0.9	0.6	0.5	0.3

428

429 Figure 4. (a) Representative cases of shape descriptors are shown using the left arcuate fasciculus as
430 an example. (b) Median values of shape descriptors across 44 subjects are listed for each association
431 pathway. The red colors are those with relatively large values in comparison with other pathways.

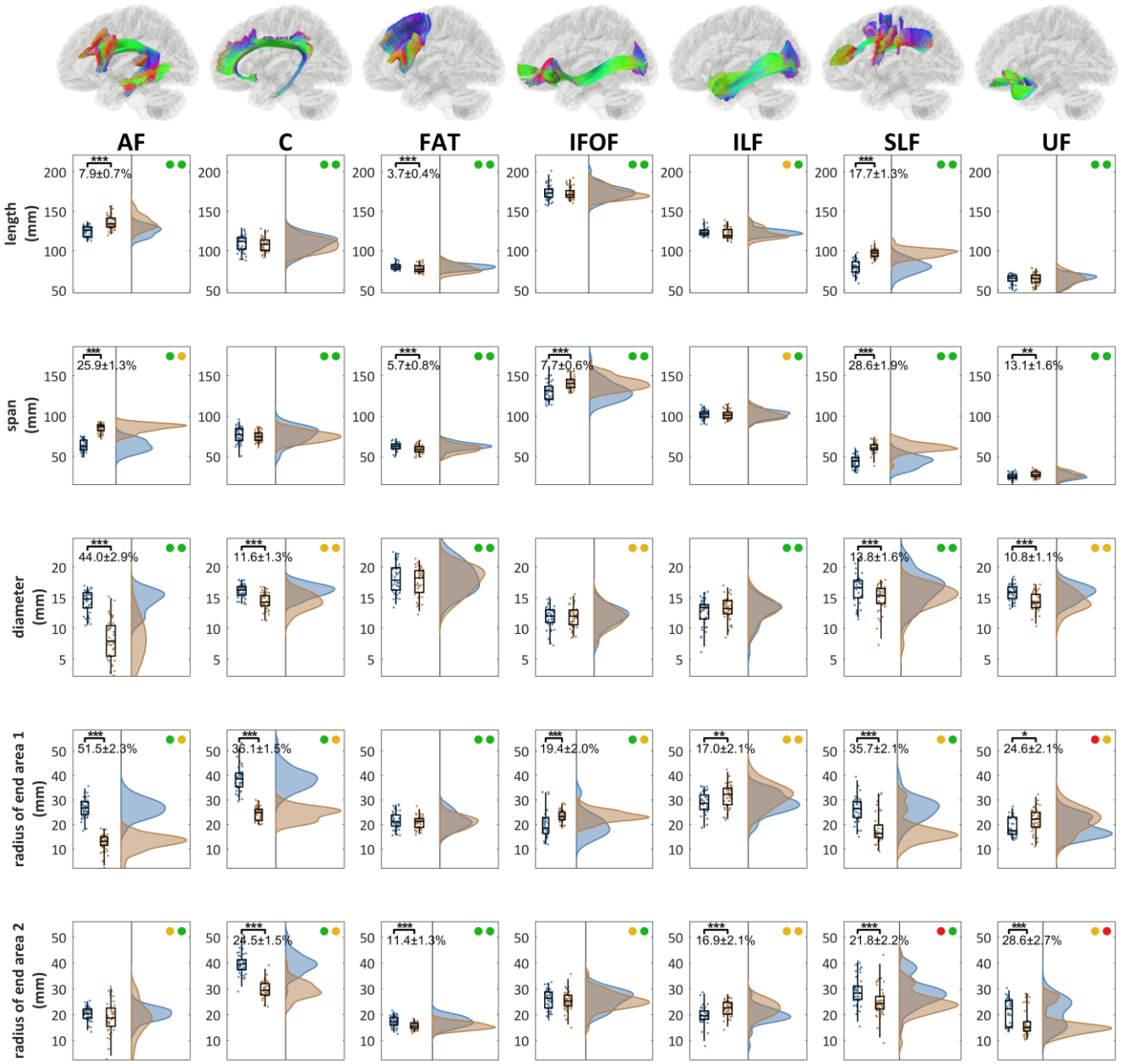

Figure 5. The distribution of the length metrics and their left-right differences in the association pathways. The association pathways present different significance level of the left-right differences (p-value: *** < 0.001, **< 0.01, *< 0.05). The test-retest reliability of the metrics for the left and right bundle is presented by colored circles (green: ICC≥0.75, yellow: 0.75>ICC≥0.5, red: ICC<0.5). The end area 1 is located at

437 the anterior end of the bundles (inferior end for frontal aslant tract). AF, C, FAT, SLF, and UF present an

438 overall left dominance in either the diameter or radius, whereas IFOF and ILF present right dominance.

439

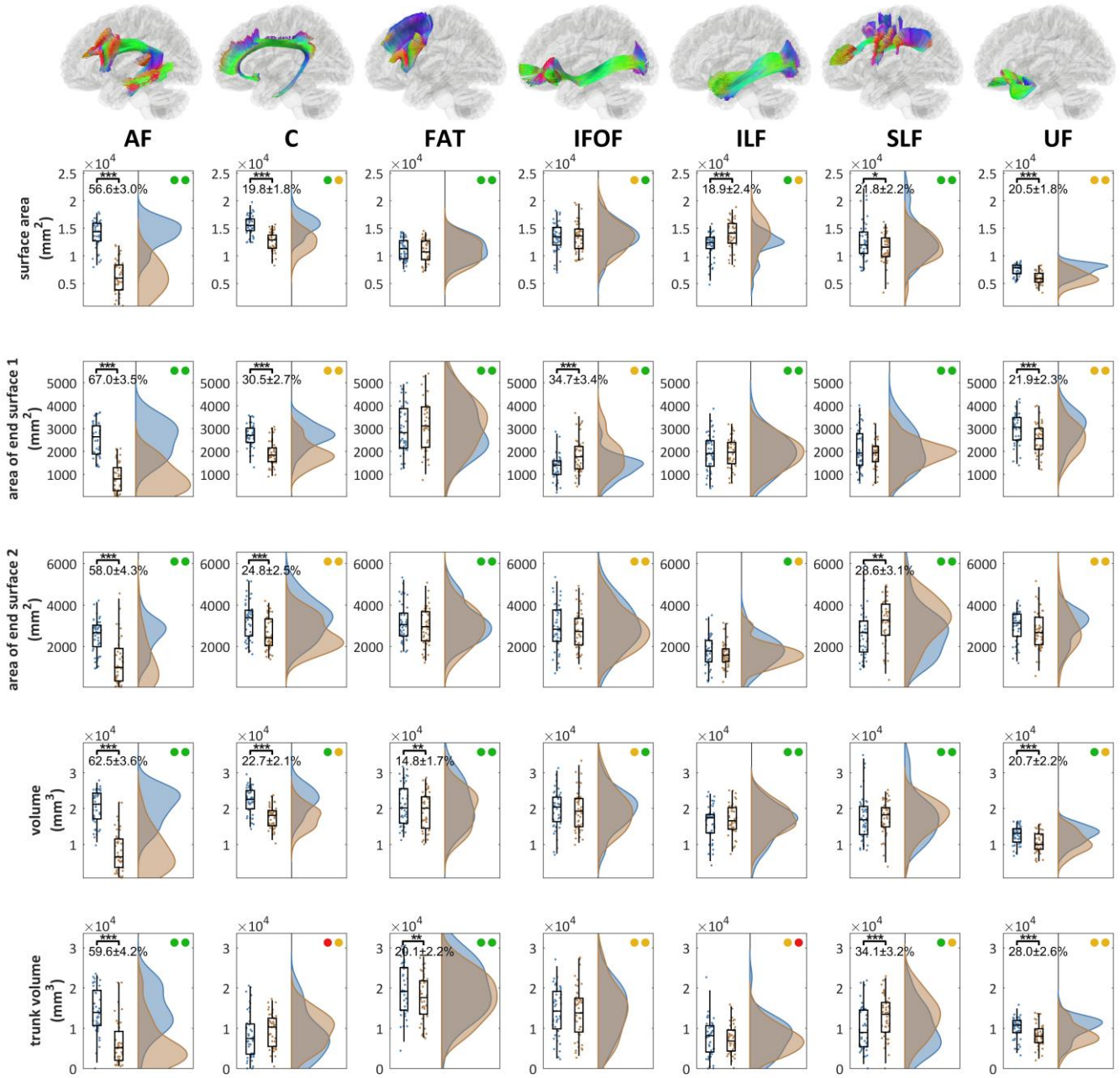

Figure 6. The distributions of the area and volume metrics and their left-right differences in the association pathways. The left-right differences are tested (p-value: *** < 0.001, ** < 0.01, * < 0.05). The test-retest reliability of the metrics for the left and right bundle is presented by colored circles (green: ICC≥0.75, yellow: 0.75>ICC≥0.5, red: ICC<0.5). The end area 1 is located at the anterior end of the bundles (inferior

445 end for frontal aslant tract). AF, C, FAT, and UF shows significant left dominance in either area or volume
446 metrics, whereas IFOF and ILF show significant right dominance. SLF presents a mixed lateralization
447 profile with either right or left dominance in different metrics.

448

449

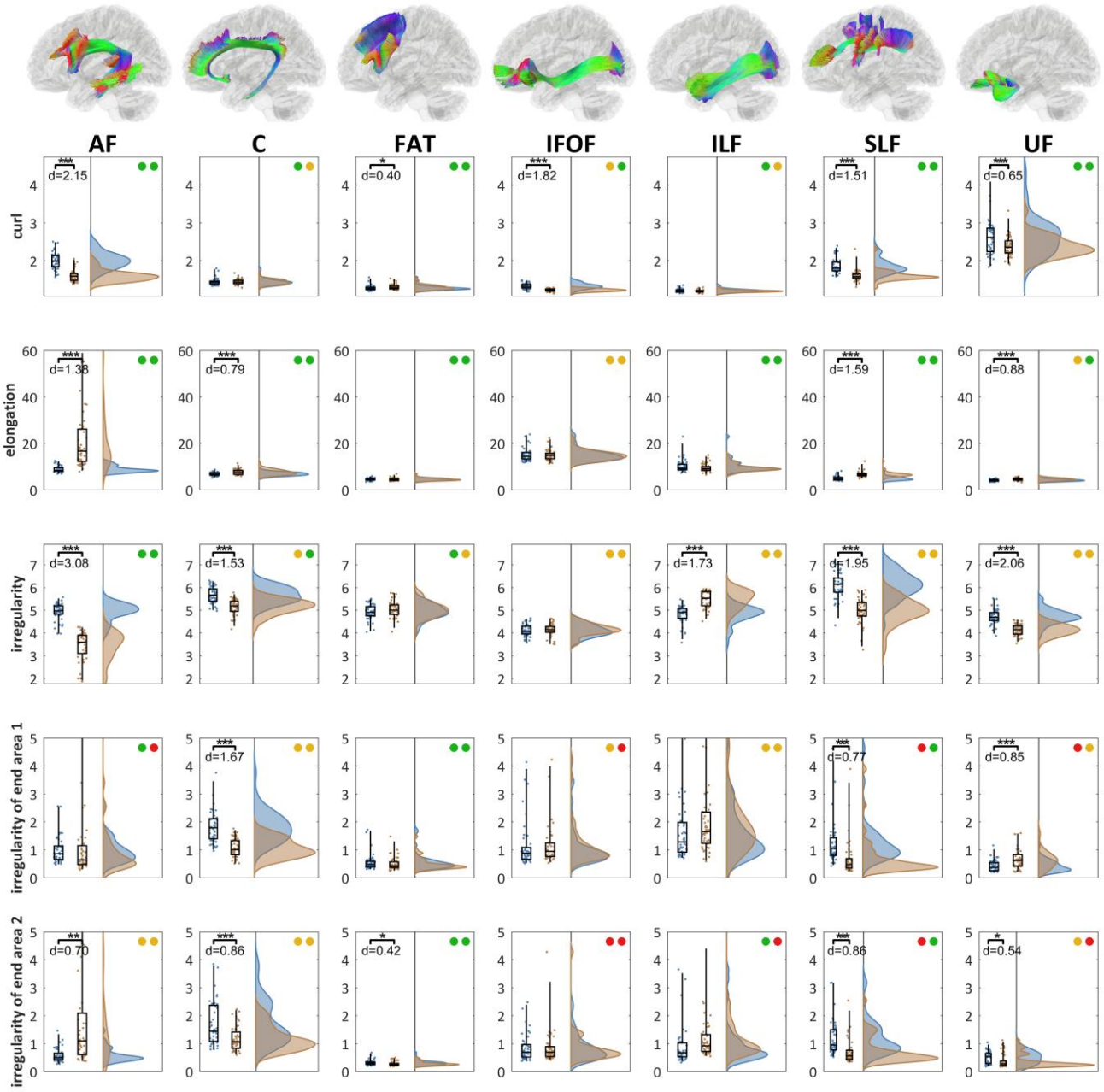

450

451 Figure 7. The distributions of the shape metrics and their left-right differences in the association pathways.

452 The left-right differences are tested (p-value: *** < 0.001, ** < 0.01, * < 0.05) and effect size (Cohen's d)

453 with test-retest reliability presented as colored circles (green: ICC≥0.75, yellow: 0.75>ICC≥0.5, red:

454 ICC<0.5). All pathways present significant lateralization at different shape metrics. The overall irregularity

455 shows the large left-dominance at AF, C, SLF, UF, and right dominance at ILF, suggesting their prominent

456 left-right differences in bundle topology.

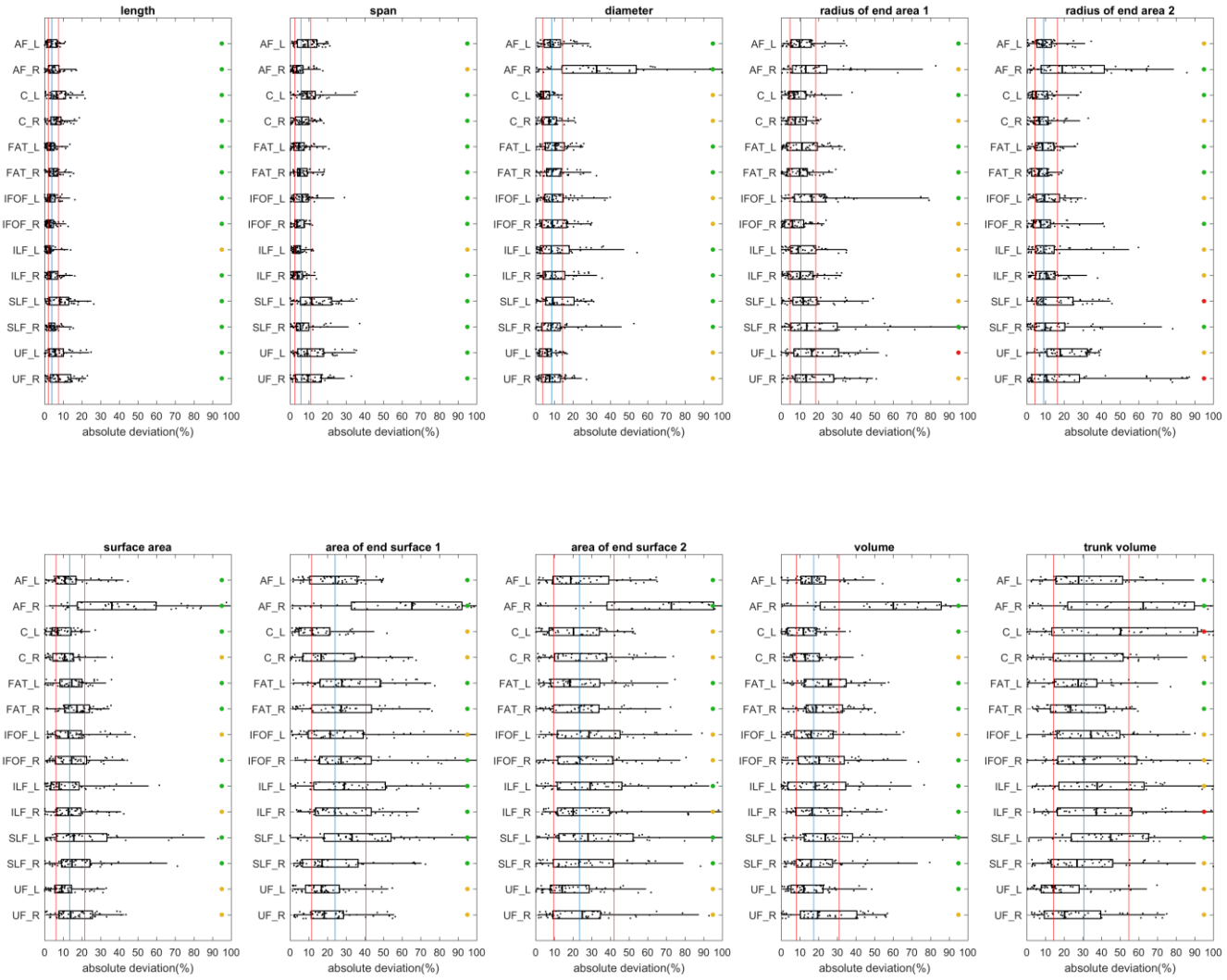

457

458 Figure 8. Between-subject variations of the length, area, and volume metrics in the association pathways.
459 The variations are quantified by absolute deviation. The blue vertical line marks the median of deviation
460 values of all bundles, whereas the two red vertical line marks the first and third quantiles. The test-retest
461 reliability is labeled by colored circles (green: ICC≥0.75, yellow: 0.75>ICC≥0.5, red: ICC<0.5). All length
462 metrics have relatively smaller between-subject variation, whereas the area and volume metrics show a
463 larger between-subject variation, particularly the area of the end surfaces showing greater than >20%
464 deviation.

Table 1: List of shape descriptors and their definition

Descriptors	Definition
Length (mm)	$\frac{1}{n}\sum_{i=1}^{i=n}\sum_{t=1}^{t=m_i-1}\|v_i(t)-v_i(t+1)\|_2$
Span (mm)	$\sum_{i=1}^{i=n}\|v(1)-v(m_i)\|_2$
Diameter (mm)	$2\sqrt{\frac{volume}{\pi \times length}}$
Radius (mm)	$\frac{1.5}{N_e}\sum_{i=1}^{i=N_e}\left\|E_i-\frac{1}{N_e}\sum_{j=1}^{j=N_e}E_j\right\|_{i\,2}$
Surface Area (mm^2)	$N_s \times voxel\ spacing^2$
Volume (mm^3)	$N \times voxel\ volume$
Trunk Volume (mm^3)	$N_t \times voxel\ volume$
Curl	$\frac{length}{span}$
Elongation	$\frac{length}{diameter}$
Irregularity of the bundle surface	$\frac{surface\ area}{\pi \times diameter \times length}$
Irregularity of the end surface	$\frac{\pi \times radius^2}{area\ of\ the\ end\ surface}$

Length metrics Area metrics Volume metrics

Bundle: trajectory form=$\{v_i(t) \mid i = 1,2,3,\dots n\}$, voxelized form=$\{V_i \mid i = 1,2,3,\dots N\}$

End surface: voxelized form=$\{E_i \mid i = 1,2,3,\dots N_e\}$

N_t is the number of "trunk bundle" voxels.

N_s is the number of tract surface voxels.

465